UNIVERSITY of York

This is a repository copy of *Quantum Rescaling, Domain Metastability, and Hybrid Domain-Walls in 2D CrI3 Magnets*.

White Rose Research Online URL for this paper:
https://eprints.whiterose.ac.uk/id/eprint/169775/

Version: Accepted Version

Article:
Wahab, Dina Abdul, Augustin, Mathias, Valero, Samuel Manas et al. (9 more authors) (2020) Quantum Rescaling, Domain Metastability, and Hybrid Domain-Walls in 2D CrI3 Magnets. Advanced Materials. 2004138. ISSN: 0935-9648

https://doi.org/10.1002/adma.202004138

Reuse
Items deposited in White Rose Research Online are protected by copyright, with all rights reserved unless indicated otherwise. They may be downloaded and/or printed for private study, or other acts as permitted by national copyright laws. The publisher or other rights holders may allow further reproduction and re-use of the full text version. This is indicated by the licence information on the White Rose Research Online record for the item.

Takedown
If you consider content in White Rose Research Online to be in breach of UK law, please notify us by emailing eprints@whiterose.ac.uk including the URL of the record and the reason for the withdrawal request.

White Rose university consortium
Universities of Leeds, Sheffield & York

eprints@whiterose.ac.uk
https://eprints.whiterose.ac.uk/

arXiv:2011.02732v1 [cond-mat.mes-hall] 5 Nov 2020

Quantum rescaling, domain metastability and hybrid domain-walls in two-dimensional CrI_3 magnets

Dina Abdul Wahab[1], Mathias Augustin[1], Samuel Manas Valero[2], Wenjun Kuang[3], Sarah Jenkins[4], Eugenio Coronado[2], Irina V. Grigorieva[3], Ivan J. Vera-Marun[3], Efrén Navarro-Moratalla[2], Richard F. L. Evans[4], Kostya S. Novoselov[3,5,6] & Elton J. G. Santos[7,†]

[1]*School of Mathematics and Physics, Queen's University Belfast, BT7 1NN, UK*

[2]*Instituto de Ciencia Molecular, Universidad de Valencia, Calle Catedrático José Beltrán 2, 46980 Paterna, Spain*

[3]*School of Physics, University of Manchester, Oxford Road, Manchester, M13 9PL, UK*

[4]*Department of Physics, The University of York, York, YO10 5DD, UK*

[5]*Department of Material Science & Engineering, National University of Singapore, Block EA, 9 Engineering Drive 1, 117575, Singapore*

[6]*Chongqing 2D Materials Institute, Liangjiang New Area, Chongqing 400714, China*

[7]*Institute for Condensed Matter Physics and Complex Systems, School of Physics and Astronomy, The University of Edinburgh, EH9 3FD, UK.*

[†]*Corresponding author: esantos@ed.ac.uk*

Higher-order exchange interactions and quantum effects are widely known to play an important role in describing the properties of low-dimensional magnetic compounds. Here we identify the recently discovered two-dimensional (2D) van der Waals (vdW) CrI_3 as a quantum non-Heisenberg material with properties far beyond an Ising magnet as initially assumed.

We find that biquadratic exchange interactions are essential to quantitatively describe the magnetism of CrI_3 but requiring quantum rescaling corrections to reproduce its thermal properties. The quantum nature of the heat bath represented by discrete electron-spin and phonon-spin scattering processes induced the formation of spin fluctuations in the low temperature regime. These fluctuations induce the formation of metastable magnetic domains evolving into a single macroscopic magnetization or even a monodomain over surface areas of a few micrometers. Such domains display hybrid characteristics of Néel and Bloch types with a narrow domain wall width in the range of 3-5 nm. Similar behaviour is expected for the majority of 2D vdW magnets where higher-order exchange interactions are appreciable.

The rediscovery of magnetism in layered vdW systems[1] has sparked an increasing interest in the investigation of spin interactions at the ultimate limit of few atom thick materials[2–11]. With the advent of new techniques of isolation, manipulation, measurements and theoretical predictions, vdW magnets have become a playground for achieving the limit of magnetism in atomically thin crystals and unveil novel physical phenomena. Implementation of 2D vdW magnets in real technologies however requires the description of their magnetic properties through an archetypal spin model such as Ising or Heisenberg. This gives a predictive indicator to what kind of behaviour is expected if such a magnet could be probed experimentally. For instance, Ising is incompatible with the appearance of magnons or spin-waves since just two spin states (e.g. $\pm z$) are taken into account[12]. If atomic spins $\mathbf{S}_i = \mu_s \mathbf{s}_i$, where μ_s is the magnetic moment, need to precess to a different spatial orientation the Heisenberg model would give unrestricted values of $\mathbf{S}_i$ on the

unit sphere surface $|\mathbf{s}_i| = 1$ in order to minimize the exchange interaction energy. As dimensionality determines the stabilization of spin ordering differently to the bulk phase, previously demonstrated for many low-dimensional nanostructures[13–15], higher-order exchange interactions beyond the Heisenberg or Ising models would be expected to play a key role in the magnetic properties of the magnetic layers. Of particular interest is CrI_3 where magnetization has been firstly measured using magneto-optical Kerr effect setup[2] at the limit of monolayer. Although CrI_3 has been treated as an Ising ferromagnet due to its large anisotropy, recent findings reporting the appearance of topological spin-excitations[16], temperature dependent magnons[17] and angle-dependent ferromagnetic resonance[18] indicate that the magnetic properties of CrI_3 are far beyond Ising.

Here we show that these puzzling features can be naturally reconciled with the inclusion of biquadratic (BQ) interactions in an extended Heisenberg framework including additional quantum rescaling corrections. Our starting point is the following spin Hamiltonian:

$$H = -\sum_{ij} J_{ij}(\mathbf{S}_i \cdot \mathbf{S}_j) - \sum_{i,j} \lambda_{ij} S_i^z S_j^z - \sum_i D_i \left(S_i^z\right)^2 - \sum_{ij} K_{ij} \left(\mathbf{S}_i \cdot \mathbf{S}_j\right)^2 \quad (1)$$

where $\mathbf{S}_i$ is the localized magnetic moment unit vector on Cr atomic sites i which are coupled by pair-wise exchange interactions. J_{ij} and λ_{ij} are the isotropic and anisotropic bilinear (BL) exchanges, respectively, and D_i is the onsite magnetic anisotropy. We used up to third-nearest neighbors on both J_{ij} and λ_{ij}. The fourth term represents a biquadratic (BQ) exchange which occurs due to the hopping of more than one electron between two adjacent sites[13,19]. Its strength is given by the constant K_{ij}, which is the simplest and most natural form of non-Heisenberg coupling. We can determine K_{ij} by calculating the energetic variation of the spins $\mathbf{S}_i$ at each Cr site at different rotation angle θ including spin-orbit coupling[20–22] (Figure 1**a**). See Supplementary Sections S1-S4

for details, and comparison with other models, such as Kitaev[23,24]. It is noteworthy that λ_{ij} and K_{ij} in monolayer CrI_3 have close magnitudes but are slightly smaller than J_{ij} (Supplementary Table S1). Indeed, in materials where the exchange is for some reason weak due to different processes, such as competition between ferromagnetic and antiferromagnetic exchange[25], BQ exchange has a particularly strong influence as observed for several different compounds[14,26–29]. This seems to be the case for most of the vdW magnets as recently demonstrated[19]. We can apply similar analysis to bulk CrI_3 which shows the same magnitude of BQ exchange for the intra-layer interactions but smaller for the interlayer counterparts (Supplementary Table S1). These results indicate that higher-order exchange processes involving two or more electrons are important in CrI_3 magnets despite of the dimensionality. Nevertheless, we focus on the effect of BQ exchange on the magnetic features of CrI_3 not considering higher order interactions, i.e. three-site spin interactions[30].

To simulate the temperature and dynamic properties of CrI_3 at a macroscopic level, we have implemented the BQ exchange interactions shown in Eq.1 within the Monte Carlo Metropolis algorithm[31] also taking into account contributions from the next-nearest neighbours. See Supplementary Sections S5 for details. In this Monte Carlo model we assume a classical spin vector $\mathbf{S}_i$ on each atomic site i of fixed length μ_s whose direction can vary freely in 3D space. The quantization vector for the spin is a local quantity which naturally includes the effects of local thermal spin fluctuations and magnon processes. This clearly separates classical and quantum contributions to the magnetic behaviour of CrI_3. To analyse whether the Ising or the non-Heisenberg model (Eq.1) provides the best description of the magnetic properties of bulk and monolayer CrI_3, we undertake a quantitative comparison between both models with the measurement of the magnetization

M versus temperature T using first-principles parameters as input. We use the magneto-optical Kerr effect (MOKE) data extracted from Ref.[2] for monolayer CrI_3, and superconducting quantum interference device (SQUID) technique for bulk CrI_3 (Supplementary Sections S6 and S7). Figure 1**a-b** show the simulated temperature dependence of the magnetization of bulk and monolayer CrI_3 relative to the experimental data. It is clear that the Ising model grossly overestimates the measured Curie temperature (T_C) for both systems by several tens of Kelvins reaching high temperatures. Ising gives $T_C \sim$200 K and $T_C \sim$102 K for bulk and monolayer CrI_3, respectively, which is also in disagreement with previous experimental studies[2,32–34]. This suggests that a single quantization axis where spins are allowed to take only two values parallel or anti-parallel to the surface is not accurate enough to represent the magnetic properties of CrI_3 magnets. Conversely, the non-Heisenberg model gives a sound agreement with the measurements resulting in Curie temperatures of 44.4 K and 62.2 K for monolayer and bulk CrI_3, respectively. We have also checked whether other models can give a sound description of the magnetic properties of CrI_3. Namely, a Heisenberg model without the inclusion of BQ interactions[35], a Kitaev model[23,24], and also the BQ model in Eq.1 including non-collinear spin-textures at the level of Dzyaloshinskii-Moriya interactions (DMI). See Supplementary Sections 4 and 8 for details. While DMI do not give any variation of T_C relative to the initial BQ model, both the Heisenberg and Kitaev models significantly underestimate the magnitude of the critical temperatures by several tens of Kelvin's relative to the measurements ($T_{\mathrm{C}}^{Kitaev} = 17.2$ K, $T_{\mathrm{C}}^{Heisenberg} = 23 - 37.4$ K). These results suggested that BL models are insufficient to describe the magnetic features of CrI_3. Furthermore, the inclusion of BQ exchange has recently been observed in the description[19] of neutron scattering measurements

on the magnon spectra of CrI_3[16]. Even though the gap opening at the Dirac point is due to the presence of Dzyaloshinskii-Moriya interactions (DMI), the interplay between BQ exchange and DMI plays a substantial role in several features observed in the spin waves at different **k**-points[36,37]. In particular at the magnon dispersion at the K−M−K path at the Brillouin zone[19]. These findings provide further background on the effect of BQ exchange on the magnetic properties of CrI_3.

The shape of $M(T)$ obtained from the classical Monte Carlo simulations instead of Eq.1 shows a much stronger curvature than displayed by the measured data at low temperatures. To better reflect the quantum nature of the heat bath of the CrI_3 systems, we apply quantum rescaling methods[38] to adjust the average strength of the thermal spin fluctuations within the non-Heisenberg model. The method has previously been applied to quantitatively describe the temperature dependent magnetization of Fe, Co, Ni and Gd magnets. We extend the approach to monolayer and bulk CrI_3 (Fig. 1**c**). Physically the temperature rescaling represents the quantum nature of the heat bath, consisting of discrete electron-spin and phonon-spin scattering processes. At low temperatures the spin directions are dominated by exchange interactions preferring ferromagnetic alignment of localized Cr spins. In the case of electron-spin scattering, only energetic electrons are inelastically scattered causing a local spin flip, while low energy electrons are elastically scattered and no spin flip occurs. Macroscopically this significantly reduces the average strength of the thermal spin fluctuations within the simulation which we approximate by applying a simple temperature rescaling of the form:

$$T_{sim} = (T_{exp}/T_C)^{1/\alpha} \tag{2}$$

where α is a phenomenological rescaling exponent extracted from the experimental data (Fig. 1**c**).

The fitting assumes a simple Curie-Bloch interpolation of the form:

$$m(T) = [1 - (T/T_C)^{\alpha}]^{\beta} \tag{3}$$

and is seen to fit a wide range of ferromagnetic and antiferromagnetic materials including the current material of interest, CrI_3. Practically our rescaling approach is only applicable over an ensemble average of hundreds of spins as individual scattering events are not directly simulated within our semi-classical method, but effectively introduce the quantum nature of the heat bath within a classical model. Nevertheless, the ability of the classical non-Heisenberg model to quantitatively reproduce the temperature dependent properties of bulk CrI_3 is remarkable. Figure 1**d** highlights the difference between simulations with and without quantum rescaling corrections for bulk CrI_3. It is clear that the classical nature of the atomistic spin model[39] induced discrepancies with the measured data below T_C. As the spins are treated classically using a non-Heisenberg Hamiltonian, which follows the Boltzmann distribution, the curvature of the measured $M(T)$ deviates from the classical behaviour due to infinitesimal thermal fluctuations of the spins at the low temperature regime. These fluctuations of the magnetization have a quantum origin that are better represented using quantum statistics within the Bose-Einstein distribution.

By fitting Eq. 3 to the bulk experimental data with $\beta_{\text{bulk}} \sim 0.25$ initially extracted from the classical simulation we obtain excellent agreement between the scaled and measured $M(T)$ for $T < T_C$ at $\alpha = 1.70$. For the monolayer data (Fig. 1**e**) we follow the same process as for the bulk, computing $\beta_{\text{1L}} = 0.22$ from first principles and Monte Carlo calculations. Assuming that the Bloch exponent α is independent of dimensionality, we find a sound agreement with the measured data for monolayer CrI_3. The different β values compared to bulk ferromagnets indicate the criticality

of the magnetization near the Curie temperature, and are not universal properties of Heisenberg and Ising systems in contrast with previous studies[32]. The Bloch exponent and therefore quantum corrections are sufficient to explain the different shapes of $M(T)$ curves without the need to resort to fundamentally different models, for example Ising, Kitaev, or XY models (Supplementary Section 4). We also performed quantitative comparison between simulated and measured data for $M(T)$ at different magnitudes of the magnetic field B_z (Fig. 1**f**). The applied B_z reduces the criticality of the magnetization close to the Curie temperature, and the simulations converge towards the experimental data mainly for temperatures below T_C with negligible differences (less than 1%.) Moreover, the field dependence of the magnetization above the Curie point is stronger in the experiments compared to the simulations since we do not take into account quantum rescaling effects above T_C. The roughly double amount of B_z in the simulations to reproduce the experimental dependence beyond the Curie point suggests that quantum effects are still important as spin wave excitations or magnons may be present as previously observed in other magnetic materials[40,41]. In reality an externally applied field affects the microscopic spin fluctuations and therefore alters the thermodynamic distribution of spins, for thin magnets it leads to a larger equilibrium magnetization than for the purely classical approach even far above T_C[40].

An outstanding question raised by the experiments is why a macroscopic magnetization or a monodomain exists in a 2D system after zero-field cooling. It is known that magnetic anisotropy overcomes the limit of the Mermin-Wagner theorem by symmetry breaking, but one would ordinarily expect that magnetic domains are stable in the system, particularly in high-anisotropy materials such as CrI_3. To investigate this we simulated the zero-field and field cooling processes

for a large square nano-flake of monolayer CrI_3 of dimensions 0.4 μm $\times$ 0.4 μm using atomistic spin dynamics (see Supplementary Section 5). The system is thermally equilibrated above the Curie temperature and then linearly cooled to 0 K in a simulated time of 2 ns for different values of applied external magnetic field, as shown in Figure 2 and Supplementary Movies S1-S3. From the simulations we extract the time evolution of the spins and the formation of magnetic domains extracting snapshots of the spin configurations during the zero-field cooling process. For zero magnetic field shown in Fig. 2**a-c** we find that the magnetic domains are metastable (Supplementary Movie S1) while for a small field of B_z =10 mT the domains are mostly removed during the 2 ns cooling process (Fig. 2**d-f**, Supplementary Movie S2). For the zero field cooling the domains persist until the end of the simulation, but show a continuous evolution in time at 0 K showing their metastable nature. As the field increases to 50 mT (Supplementary Movie S3) the domains are flushed out with a homogeneous magnetization being observed over the entire simulation area (0.4 μm $\times$ 0.4 μm) after 2 ns. Our observations suggest that magnetic domains are not intrinsically stable in CrI_3, which indicates a macroscopic magnetization throughout the surface even in zero-magnetic field. Domains as large as 0.57 μm have been observed (Supplementary Movie S1). Moreover, the interplay between metastability and large magnetic anisotropy could give the physical ingredients for the coexistence of different domain wall types in CrI_3. This effect could be intrinsic to 2D vdW magnets with wide implications for device developments and real applications.

Interestingly, the metastability of the domains prevents the wall profiles from reaching a truly ground-state configuration. A projection of the magnetization **M** over the domain walls at 0 K and zero field (Fig. 2**g**) shows that such unstable magnetic domains can be of several types

(Fig. 2**h-k**). This is particularly acute near the middle of the sample where quenching leads to a frustrated set of domains and the in-plane direction of the magnetizations rotates repeatedly. This effect is also observed closer to the edge where it is possible to observe a persistent rotation of the in-plane magnetization (Fig.2**k**) over short lengths of the wall but extending over the entire boundary of the magnetic domains. For the few domain walls that can be stabilized at a specific magnetization direction we find that the majority of the magnetic domain walls in CrI_3 (around 97%) are Néel-type (Fig. 2**i**) but with some large proportion of a new hybrid type (Fig. 2**h**) with characteristics between Bloch (Fig. 2**j**) and Néel walls. A minor amount of domains, less than 3%, stabilized at Bloch type over the entire system. These domains were obtained from different stochastic realizations of the zero field cooling simulations.

To determine whether such diverse domain walls have additional characteristics in monolayer CrI_3, we project the total magnetization at the wall over in-plane (M_x, M_y) and out-of-plane (M_z) components (Fig. 3**a**, **c e**). While M_z through Bloch, hybrid and Néel domains does not change appreciably, both M_x and M_y show different behaviour characterizing a specific kind of domain wall with its specific spin orientations (Fig. 3**b**, **d f**). It is noteworthy that the hybrid domains have a different chirality for the in-plane moments relative to Bloch and Néel with a sizable component along of the y axis as the spins transition from one domain to another (Fig. 3**c**,**d** and Fig. 2**h**). We can extract the domain wall width δ by fitting the different components of the magnetization (M_x, M_y, M_z) to a standard equation profile of the form:

$$M(r) = \tanh(\pi(r - r_0)/\delta) \tag{4}$$

where r_0 is the domain wall position at a specific orientation (x, y, z). All types of wall have a

very narrow domain wall width of around $\delta \sim 3.8 - 4.8$ nm (Fig. 3**a**,**c**,**e**). Such small domain walls are typically only seen in permanent magnetic materials due to the exceptionally high magnetic anisotropy[42]. For such materials the magnetic domains are stabilized in a zero-remanence state after zero-field cooling due to the long-ranged dipole-dipole interactions which are also taken into account in our calculations (Supplementary Section S9). Nevertheless we find that this is not the case for monolayer CrI_3 which suggests that this material reunites features from a soft-magnet (e.g. easy movement of domain walls, small area hysteresis loop) and a hard-magnet (e.g. relative high magnetocrystalline anisotropy, narrow domain walls).

The variety of domain-walls observed in CrI_3 can be directly related to the magnetic stability of the layer[42]. For magnetic materials with strong uniaxial anisotropy, the equilibrium state is normally reached beyond the field cooling process[43]. Even though no thermal energy would be available at such limit, the spins would still evolve to stabilize the ground-state via the minimization of other contributions of the total energy, e.g. exchange, anisotropy. This process can be observed in Figure 4 for the time-evolution of one of the spin dynamics of monolayer CrI_3 once the system had achieved 0 K within 2.0 ns at zero field. There is a continuous modification of the domain-wall profiles through all components of the magnetization ($M_{x,y,z}$) over time. The variations on M_z across the magnetic domains (Fig. 4**a-b**) tend to be smooth without sudden changes differently to those observed along the in-plane components (Fig. 4**c-d**). For them, several peaks appeared and vanished on a time scale of few tenths of nanoseconds indicating the stochastic nature of the spin-fluctuations in the system. Indeed, we observed such random fluctuations of $M_{x,y}$ even beyond 20 ns which suggest that the system may be intrinsically not a local minimum but rather at

a flat energy landscape. We can extract some qualitative information about the magnetic behaviour of the domains in CrI_3 regarding stability and domain size using magnetic force microscopy (MFM) experiments (see Supplementary Section S10 for details). Supplementary Figures S18-S19 shows a zero-field cooled CrI_3 thick flake (0.04 μm) with lateral dimensions of approximately 4 μm $\times$ 2 μm at 4.2 K where magnetic domains of about 2 μm persist to the base temperature (Supplementary Fig. S19**a-b**). Even though the measurements were undertaken at a sample area one order of magnitude larger than that utilized in the simulations (e.g. 0.16 μm^2), the magnetic domains formed in both theory and experiments still keep the same scale relative to the domain size created. This indicates that mostly a monodomain is created over the entire surface as suggested by the theoretical results. Moreover, the topography of the domains extracted from frequency shift profiles (Suppl. Fig. S19**f-i**) clearly shows sharp domain walls (e.g. smaller than 20 nm) but the resolution limitation of the MFM technique (50 nm diameter of an average Cr coated MFM tip) prevents the direct comparison with the sub-10 nm prediction extracted from theory. Similar limitation ($\sim$40-60 nm) was also observed in recent measurements using a scanning single-spin magnetometry with a Nitrogen-Vacancy (NV) centre spin in the tip of an atomic force microscope[44] and a magnetic-circular dichroism technique[45]. This indicates that further development on the experimental side is needed to further validate the simulation results. It is worth mentioning that even though the time-scale used in the spin dynamics spans around 20 ns, it reproduces accurately the domain structure obtained via MFM over a few hours scan process. The images recorded in Supplementary Figure S19 may be considered as the final magnetic state as several electronic and spin interactions take place. The early stages which determined the magnetic ordering can be

extracted from the micro-magnetic simulations as a sound agreement is obtained with the recorded MFM images. In addition, atomistic simulations undertake in bulk CrI_3 (Supplementary Figure S20) support the picture that magnetic domains are more stable in bulk (Supplementary Figures S18-S19) than in monolayer due to the additional interlayer interactions driven by vdW forces and spin exchange. Thus, the meta-stability of the magnetic domains seems to be more present in the lower dimensionality of single sheets.

The magnetism of 2D materials at the limit of one or few layers is still at its early stages with rich phenomena yet to be explored. The demonstration here of quantum effects in CrI_3 together with its non-Heisenberg character due to higher-order exchange interactions should motivate significant future studies to understand both the mechanism of the computed enhancement of bi-quadratic interactions and to confirm that such effect may be general to several families of 2D vdW magnets. In addition, the metastability of the magnetic domains in CrI_3 induces a homogeneous magnetization or even a single domain over the entire surface. This behavior associated with the out-of-plane anisotropy and the higher coercivity of CrI_3 indicates a potential magnetic media for perpendicular recording. It is still unclear however which kind of domain motion can be foreseen in such thin layered compound, and how the coexistence of different domain types can affect device architectures. This suggests new routes for magnetic-domain engineering at the atomic limit.

Supplementary Materials

Materials and Methods.

Supplementary sections S1 to S11, movies S1, S2, S3 and Figs. S1 to S20.

0.0.1 Data Availability

The data that support the findings of this study are available within the paper and its Supplementary Information.

0.0.2 Competing interests

The Authors declare no conflict of interests.

0.0.3 Acknowledgments

RFLE gratefully acknowledges the financial support of the Engineering and Physical Sciences Research Council (Grant No. EPSRC EP/P022006/1) and the use of the VIKING Cluster, which is a high performance compute facility provided by the University of York. This work was enabled by code enhancements to the VAMPIRE software implemented under the embedded CSE programme (ecse0709) and (ecse1307) of the ARCHER UK National Supercomputing Service. EJGS acknowledges computational resources through the UK Materials and Molecular Modelling Hub

for access to THOMAS supercluster, which is partially funded by EPSRC (EP/P020194/1); CIRRUS Tier-2 HPC Service (ec131 Cirrus Project) at EPCC (http://www.cirrus.ac.uk) funded by the University of Edinburgh and EPSRC (EP/P020267/1); ARCHER UK National Supercomputing Service (http://www.archer.ac.uk) via Project d429. EJGS acknowledges the EPSRC Early Career Fellowship (EP/T021578/1) and the University of Edinburgh for funding support. ENM acknowledges the European Research Council (ERC) under the Horizon 2020 research and innovation programme (ERC StG, grant agreement No. 803092).

0.0.4 Author Contributions

EJGS conceived the idea and supervised the project. MA and DAW performed ab initio and Monte Carlo (MC) simulations under the supervision of EJGS. RFLE implemented the biquadratic exchange interactions in VAMPIRE, and also undertook MC simulations. SJ implemented the atomistic dipole-dipole solver to verify the computed domain wall profiles. EVM and SMV fabricated and characterized the samples. IJVM, WK, KSN measured the samples using SQUID. EVM, SMV, EC performed the MFM measurements. EVM, IJVM, IVG, KSN analyzed the data and contributed to the discussions. EJGS wrote the paper with inputs from all authors. All authors contributed to this work, read the manuscript, discussed the results, and agreed to the contents of the manuscript.

References and Notes

1. de Jongh, L. *Magnetic Properties of Layered Transition Metal Compounds* (Springer, 2012).

2. Huang, B. *et al.* Layer-dependent ferromagnetism in a van der waals crystal down to the monolayer limit. *Nature* **546**, 270 EP – (2017). URL https://doi.org/10.1038/nature22391.

3. Gong, C. *et al.* Discovery of intrinsic ferromagnetism in two-dimensional van der waals crystals. *Nature* **546**, 265–269 (2017). URL http://dx.doi.org/10.1038/nature22060. Letter.

4. Song, T. *et al.* Giant tunneling magnetoresistance in spin-filter van der waals heterostructures. *Science* **360**, 1214–1218 (2018). URL http://science.sciencemag.org/content/360/6394/1214. http://science.sciencemag.org/content/360/6394/1214.full.pdf.

5. Klein, D. R. *et al.* Probing magnetism in 2d van der waals crystalline insulators via electron tunneling. *Science* **360**, 1218–1222 (2018). URL http://science.sciencemag.org/content/360/6394/1218. http://science.sciencemag.org/content/360/6394/1218.full.pdf.

6. Ghazaryan, D. *et al.* Magnon-assisted tunnelling in van der waals heterostructures based on crbr3. *Nature Electronics* **1**, 344–349 (2018). URL https://doi.org/10.1038/s41928-018-0087-z.

7. Wang, Z. *et al.* Very large tunneling magnetoresistance in layered magnetic semiconductor cri3. *Nature Communications* **9**, 2516 (2018). URL https://doi.org/10.1038/s41467-018-04953-8.

8. Fei, Z. *et al.* Two-dimensional itinerant ferromagnetism in atomically thin fe3gete2. *Nature Materials* **17**, 778–782 (2018). URL https://doi.org/10.1038/s41563-018-0149-7.

9. Seyler, K. L. *et al.* Ligand-field helical luminescence in a 2d ferromagnetic insulator. *Nature Physics* **14**, 277–281 (2018). URL https://doi.org/10.1038/s41567-017-0006-7.

10. Tian, Y., Gray, M. J., Ji, H., Cava, R. J. & Burch, K. S. Magneto-elastic coupling in a potential ferromagnetic 2d atomic crystal. *2D Materials* **3**, 025035 (2016). URL https://doi.org/10.1088%2F2053-1583%2F3%2F2%2F025035.

11. Guguchia, Z. *et al.* Magnetism in semiconducting molybdenum dichalcogenides. *Science Advances* **4** (2018). URL https://advances.sciencemag.org/content/4/12/eaat3672. https://advances.sciencemag.org/content/4/12/eaat3672.full.pdf.

12. Skomski, R. *Simple Models of Magnetism* (Oxford Graduate Texts, 2008).

13. Slonczewski, J. C. Fluctuation mechanism for biquadratic exchange coupling in magnetic multilayers. *Phys. Rev. Lett.* **67**, 3172–3175 (1991). URL https://link.aps.org/doi/10.1103/PhysRevLett.67.3172.

14. Bode, M. *et al.* Chiral magnetic order at surfaces driven by inversion asymmetry. *Nature* **447**, 190 EP – (2007). URL https://doi.org/10.1038/nature05802.

15. Rohart, S. & Thiaville, A. Skyrmion confinement in ultrathin film nanostructures in the presence of dzyaloshinskii-moriya interaction. *Phys. Rev. B* **88**, 184422 (2013). URL https://link.aps.org/doi/10.1103/PhysRevB.88.184422.

16. Chen, L. *et al.* Topological spin excitations in honeycomb ferromagnet cri_3. *Phys. Rev. X* **8**, 041028 (2018). URL https://link.aps.org/doi/10.1103/PhysRevX.8.041028.

17. Jin, W. *et al.* Raman fingerprint of two terahertz spin wave branches in a two-dimensional honeycomb ising ferromagnet. *Nature Communications* **9**, 5122 (2018). URL https://doi.org/10.1038/s41467-018-07547-6.

18. Lee, I. *et al.* Fundamental spin interactions underlying the magnetic anisotropy in the kitaev ferromagnet cri_3. *Phys. Rev. Lett.* **124**, 017201 (2020). URL https://link.aps.org/doi/10.1103/PhysRevLett.124.017201.

19. Kartsev, A., Augustin, M., Evans, R. F. L., Novoselov, K. S. & Santos, E. J. G. Biquadratic exchange interactions in two-dimensional magnets. *npj Computational Materials* **6**, 150 (2020). URL https://doi.org/10.1038/s41524-020-00416-1.

20. Hellsvik, J. *et al.* Tuning order-by-disorder multiferroicity in cuo by doping. *Phys. Rev. B* **90**, 014437–014446 (2014).

21. Fedorova, N. S., Ederer, C., Spaldin, N. A. & Scaramucci, A. Biquadratic and ring exchange interactions in orthorhombic perovskite manganites. *Phys. Rev. B* **91**, 165122–165136 (2015).

22. Novák, P., Chaplygin, I., Seifert, G., Gemming, S. & Laskowski, R. Ab-initio calculation of exchange interactions in ymno3. *Computational Materials Science* **44**, 79 – 81 (2008). URL http://www.sciencedirect.com/science/article/pii/S0927025608000669. International Conference on Materials for Advanced Technologies 2007 (ICMAT 2007) Selected papers of Symposium O: Frontiers in Computational Materials Science.

23. Kitaev, A. Anyons in an exactly solved model and beyond. *Annals of Physics* **321**, 2 – 111 (2006). URL http://www.sciencedirect.com/science/article/pii/S0003491605002381. January Special Issue.

24. Xu, C., Feng, J., Xiang, H. & Bellaiche, L. Interplay between kitaev interaction and single ion anisotropy in ferromagnetic cri3 and crgete3 monolayers. *npj Computational Materials* **4**, 57 (2018). URL https://doi.org/10.1038/s41524-018-0115-6.

25. Nagaev, É. L. Anomalous magnetic structures and phase transitions in non-heisenberg magnetic materials. *Soviet Physics Uspekhi* **25**, 31–57 (1982). URL https://doi.org/10.1070%2Fpu1982v025n01abeh004495.

26. Wysocki, A. L., Belashchenko, K. D. & Antropov, V. P. Consistent model of magnetism in ferropnictides. *Nature Physics* **7**, 485 EP – (2011). URL https://doi.org/10.1038/nphys1933.

27. Harris, E. A. & Owen, J. Biquadratic exchange between mn^{2+} ions in mgo. *Phys. Rev. Lett.* **11**, 9–10 (1963). URL https://link.aps.org/doi/10.1103/PhysRevLett.11.9.

28. Turner, A. M., Wang, F. & Vishwanath, A. Kinetic magnetism and orbital order in iron telluride. *Phys. Rev. B* **80**, 224504 (2009). URL https://link.aps.org/doi/10.1103/PhysRevB.80.224504.

29. Zhu, H.-F. *et al.* Giant biquadratic interaction-induced magnetic anisotropy in the iron-based superconductor $A_xFe_{2-y}Se_2$. *Phys. Rev. B* **93**, 024511 (2016). URL https://link.aps.org/doi/10.1103/PhysRevB.93.024511.

30. Hoffmann, M. & Blügel, S. Systematic derivation of realistic spin models for beyond-heisenberg solids. *Phys. Rev. B* **101**, 024418 (2020). URL https://link.aps.org/doi/10.1103/PhysRevB.101.024418.

31. Evans, R. F. L. *et al.* Atomistic spin model simulations of magnetic nanomaterials. *Journal of Physics: Condensed Matter* **26**, 103202 (2014). URL https://doi.org/10.1088%2F0953-8984%2F26%2F10%2F103202.

32. Liu, Y. & Petrovic, C. Three-dimensional magnetic critical behavior in cri_3. *Phys. Rev. B* **97**, 014420 (2018). URL https://link.aps.org/doi/10.1103/PhysRevB.97.014420.

33. Lin, G. T. *et al.* Critical behavior of two-dimensional intrinsically ferromagnetic semiconductor cri3. *Applied Physics Letters* **112**, 072405 (2018). URL https://doi.org/10.1063/1.5019286. https://doi.org/10.1063/1.5019286.

34. Fu, Y. K., Sun, Y. & Luo, X. Magnetic entropy scaling in two-dimensional intrinsically ferromagnetic semiconductor cri3. *Journal of Applied Physics* **125**, 053901 (2019). URL https://doi.org/10.1063/1.5079911. https://doi.org/10.1063/1.5079911.

35. Lado, J. L. & Fernández-Rossier, J. On the origin of magnetic anisotropy in two dimensional cri 3. *2D Materials* **4**, 035002 (2017). URL http://stacks.iop.org/2053-1583/4/i=3/a=035002.

36. Kim, H. H. *et al.* Evolution of interlayer and intralayer magnetism in three atomically thin chromium trihalides. *Proceedings of the National Academy of Sciences* **116**, 11131–11136

(2019). URL https://www.pnas.org/content/116/23/11131. https://www.pnas.org/content/116/23/11131.full.pdf.

37. Li, S. *et al.* Magnetic-field-induced quantum phase transitions in a van der waals magnet. *Phys. Rev. X* **10**, 011075 (2020). URL https://link.aps.org/doi/10.1103/PhysRevX.10.011075.

38. Evans, R. F. L., Atxitia, U. & Chantrell, R. W. Quantitative simulation of temperature-dependent magnetization dynamics and equilibrium properties of elemental ferromagnets. *Phys. Rev. B* **91**, 144425 (2015). URL https://link.aps.org/doi/10.1103/PhysRevB.91.144425.

39. Kuz'min, M. D. Shape of temperature dependence of spontaneous magnetization of ferromagnets: Quantitative analysis. *Phys. Rev. Lett.* **94**, 107204 (2005). URL https://link.aps.org/doi/10.1103/PhysRevLett.94.107204.

40. Qin, H. J., Zakeri, K., Ernst, A. & Kirschner, J. Temperature dependence of magnetic excitations: Terahertz magnons above the curie temperature. *Phys. Rev. Lett.* **118**, 127203 (2017). URL https://link.aps.org/doi/10.1103/PhysRevLett.118.127203.

41. Tao, X., Landau, D. P., Schulthess, T. C. & Stocks, G. M. Spin waves in paramagnetic bcc iron: Spin dynamics simulations. *Phys. Rev. Lett.* **95**, 087207 (2005). URL https://link.aps.org/doi/10.1103/PhysRevLett.95.087207.

42. *Magnetic Domains: The Analysis of Magnetic Microstructures* (Springer, 1998).

43. Wulferding, D. *et al.* Domain engineering of the metastable domains in the 4f-uniaxial-ferromagnet ceru2ga2b. *Scientific Reports* **7**, 46296 (2017). URL https://doi.org/10.1038/srep46296.

44. Thiel, L. *et al.* Probing magnetism in 2d materials at the nanoscale with single-spin microscopy. *Science* (2019). URL https://science.sciencemag.org/content/early/2019/04/24/science.aav6926. https://science.sciencemag.org/content/early/2019/04/24/science.aav6926.full.pdf.

45. Zhong, D. *et al.* Layer-resolved magnetic proximity effect in van der waals heterostructures. *Nature Nanotechnology* **15**, 187–191 (2020). URL https://doi.org/10.1038/s41565-019-0629-1.

Figure captions

Figure 1: **Quantum rescaling corrections. a-b,** Comparison of measured and calculated temperature dependent magnetization (M/M_s) of bulk and monolayer (1L) CrI_3, respectively, using Ising and non-Heisenberg models (Eq. 1). In both cases, the Ising model leads to large over-estimation of the Curie temperature (T_C) relative to the experiments. Even with the inclusion of biquadratic exchange into the description of the spin interactions, some deviations relative to the experiments are observed at low-temperatures. **c,** Plot of the effective simulation (spin) temperature against the comparable experimental temperature of the environment for different values of the phenomenological rescaling exponent α. For $\alpha = 1$ the two temperatures are equal and represents the usual situation for a classical Heisenberg magnet. For increasing values of α the effective spin temperature is reduced due to the quantum nature of the heat bath reducing the spin fluctuations. The value of $\alpha = 1.70179$ extracted from the measured data for bulk CrI_3 is shown for comparative purposes. **d,** Detailed comparison of the classical non-Heisenberg simulation and the experimental data for bulk CrI_3 at a magnetic field of $B_z = 1.0$ T. The linear behaviour of the magnetization at low temperatures is a well-known deficiency of a classical model. Applying quantum rescaling to include the quantum nature of the heat bath gives a quantitative agreement with the experimental data at the low temperature regime. At elevated temperatures, the differences arise due to the presence of an external magnetic field which resulted in values of T_C of 69 K from simulations and 63 K from experiments. **e,** Magnetization as a function of the reduced temperature (T/T_C) for monolayer CrI_3 comparing classical and quantum rescaling-corrected simulations with the experimental data. The data is plotted normalized to T_c due to the small difference between measured and calculated Curie temperatures to enable a direct comparison of the top of the magnetization curve. The fitted line to the experimental data uses the computed value of $\beta = 0.22 \pm 0.004$ from the classical simulation and assumed temperature rescaling exponent $\alpha = 1.70$ fitted from the bulk experimental data. **f,** Comparative simulations of the temperature dependent magnetization for bulk CrI_3 in different applied magnetic fields including temperature rescaling and normalized to T_C. The simulations show a sound agreement with the experimental data at temperatures less than T_C, while above T_C the apparent paramagnetic susceptibility is lower in the simulations due to an absence of quantum effects above the Curie temperature.

Figure 2: **Theory-predicted magnetic domains in monolayer CrI_3. a-c,** and **d-f,** Magnetic domain configurations obtained during field cooling at 0 mT and 10 mT, respectively. Bright and dark areas at T$\leq$ 16 K correspond to spins pointed along the easy-axis in different spin polarizations (e.g. up or down). Purple and mixed colours correspond to different spin orientations either before stabilization of the domains at T$\geq$ 16 K, or at the domain walls at T$\leq$ 16 K. As the system cools down the magnetic domains coalesce to form a circular shape to minimize the domain wall energy. Domains anti-parallel to the field direction are unstable, and eventually reverse leaving a saturated domain state at low temperatures. **g,** Analysis of the domain walls from **c,** at different parts of the crystals undertaking an in-plane projection of the magnetization $\vec{M}$ according to its colour orientation at the domain walls. A coexistence of several domain wall types is observed through **h,** Néel, **i,** Bloch, **j,** hybrid, and **k,** mixed domain walls. A continuous rotation of the spins is observed in the hybrid domains which extends from few tens of Å up to few nm's.

Figure 3: **Simulated hybrid domain-walls.** Plot of the domain wall profiles for metastable domain walls at T = 0 K for two different stochastic realizations in monolayer CrI_3. Three characteristic shapes are seen: **a-b,** Bloch type, where the in-plane magnetization (M_x, M_y) is parallel to the domain wall. **c-d,** Hybrid type, where the in-plane magnetization is between Néel and Bloch type and lies at some angle to the wall direction. **e-f,** Néel-Néel-type where the in-plane magnetization is perpendicular to the domain wall. The schematics in the right show a visualization of the individual spin directions in the domain wall. Note that the different sign of the *x* and *y* components indicates a different domain wall chirality. The out of plane magnetization (M_z) does not show appreciable modifications over the three domains observed. The calculated domain wall width is in the range of 3.8-4.8 nm. Such narrow widths are typically only found in permanent magnets such as L10-FePt nanoparticles or $Nd_2Fe_{14}B$ crystals[42].

Figure 4: **Modelling of spin fluctuations across domains. a,** Snapshot of a spin dynamics of monolayer CrI_3 obtained through zero-field cooling down process after 2.00 ns and reaching 0 K . The magnetization along of the easy-axis (M_z) is displayed showing the domain formation. Bright (dark) areas correspond to $M_z = \pm 1$, respectively. A path (dashed line) connecting three points A, B and C at the boundary between different magnetic domains is showed. **b-d,** Variations of M_z and the out-of-plane components of the magnetization (M_x, M_y), respectively, along of $A-B-C$ at different times (2.40-3.80 ns) after 0 K is obtained. The shaded areas determine the regions considered along the path.

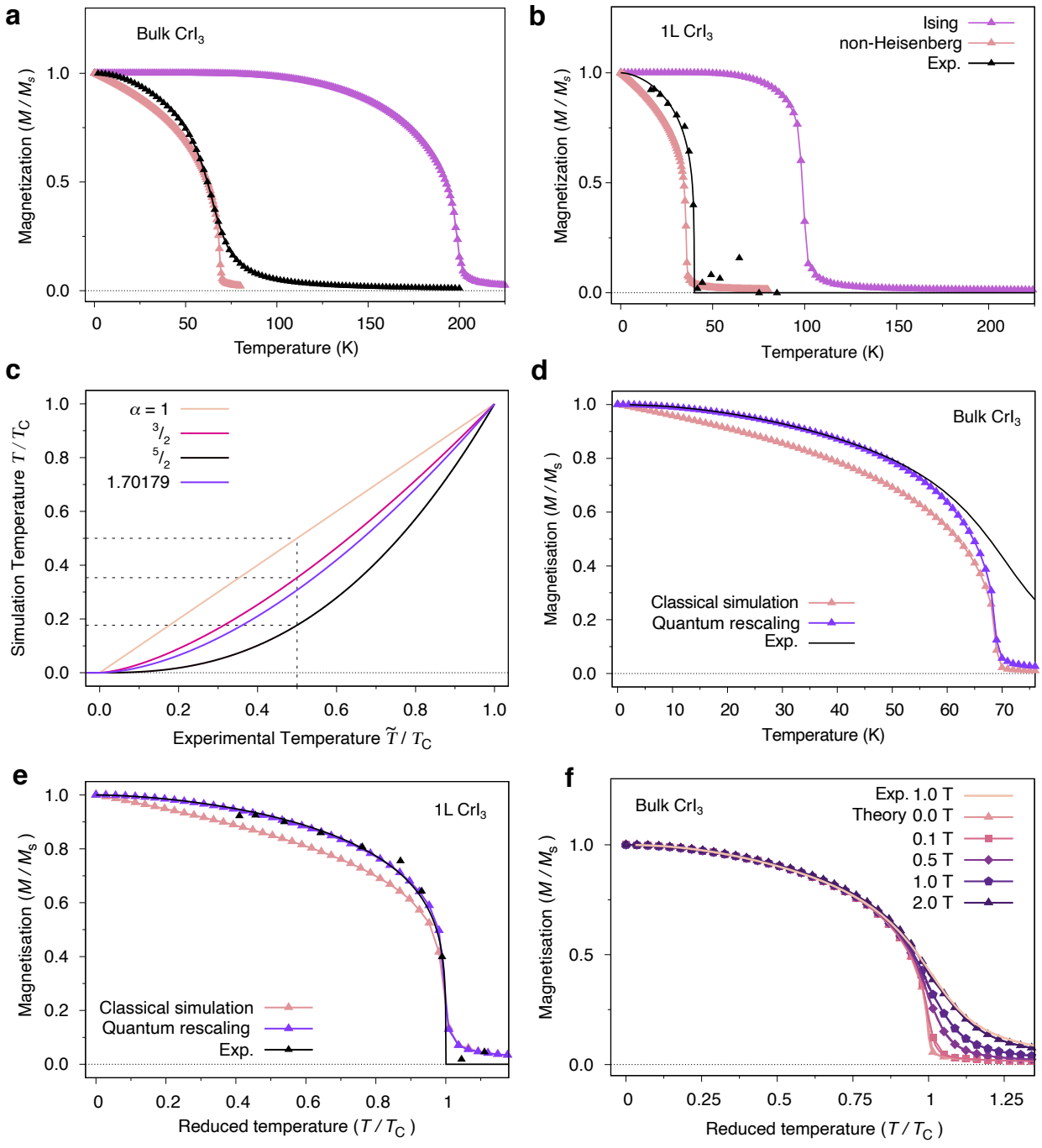
a
Bulk CrI3
Magnetization (M / Ms)
Temperature (K)
b
1L CrI3
Ising
non-Heisenberg
Exp.
Magnetization (M / Ms)
Temperature (K)
c
α = 1
3/2
5/2
1.70179
Simulation Temperature T / TC
Experimental Temperature T̃ / TC
d
Bulk CrI3
Classical simulation
Quantum rescaling
Exp.
Magnetisation (M / Ms)
Temperature (K)
e
1L CrI3
Classical simulation
Quantum rescaling
Exp.
Magnetisation (M / Ms)
Reduced temperature (T / TC)
f
Bulk CrI3
Exp. 1.0 T
Theory 0.0 T
0.1 T
0.5 T
1.0 T
2.0 T
Magnetisation (M / Ms)
Reduced temperature (T / TC)

Figure 1

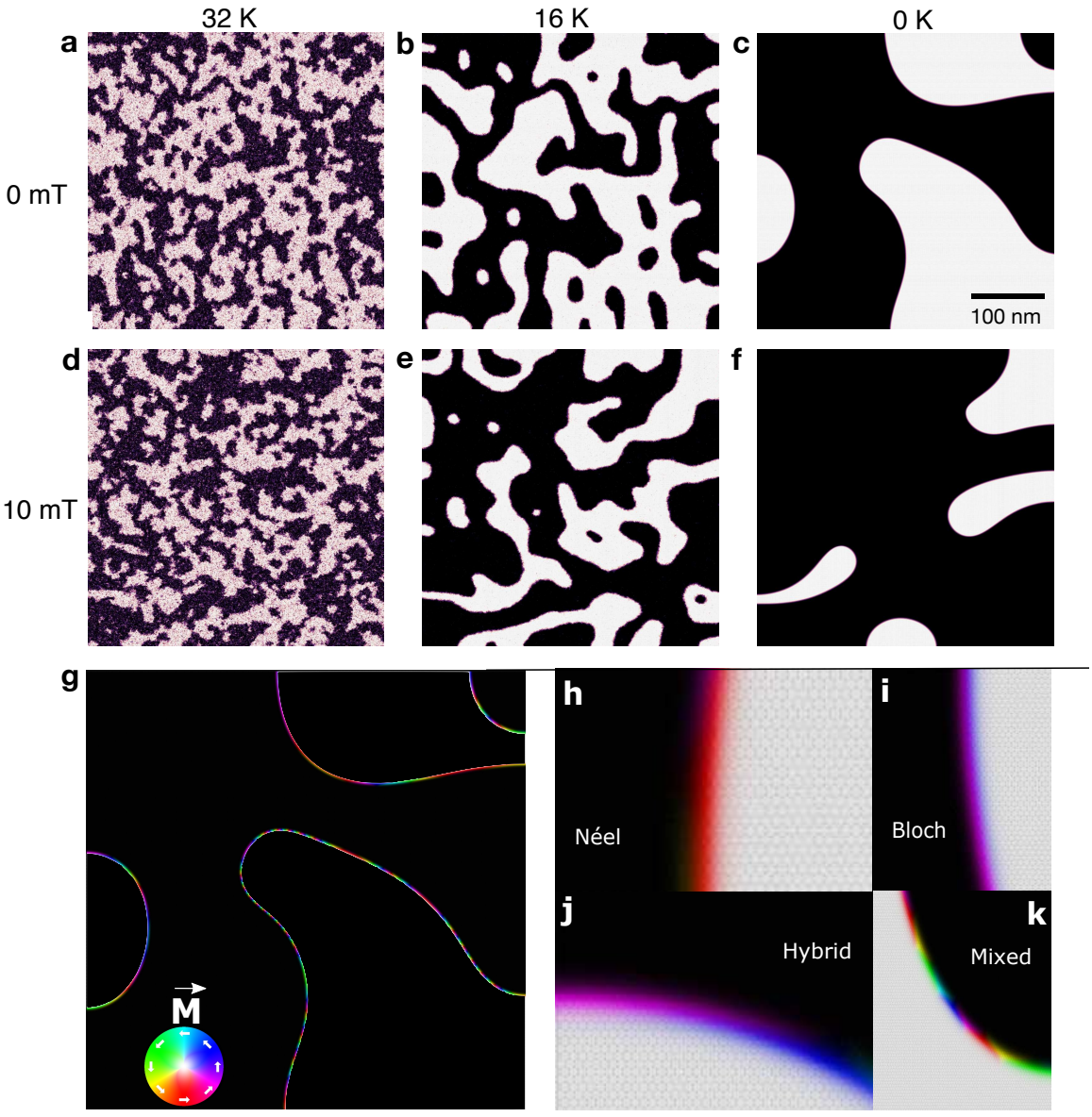
32 K
16 K
0 K
a
b
c
0 mT
100 nm
d
e
f
10 mT
g
h
i
Néel
Bloch
j
k
Hybrid
Mixed
M

Figure 2

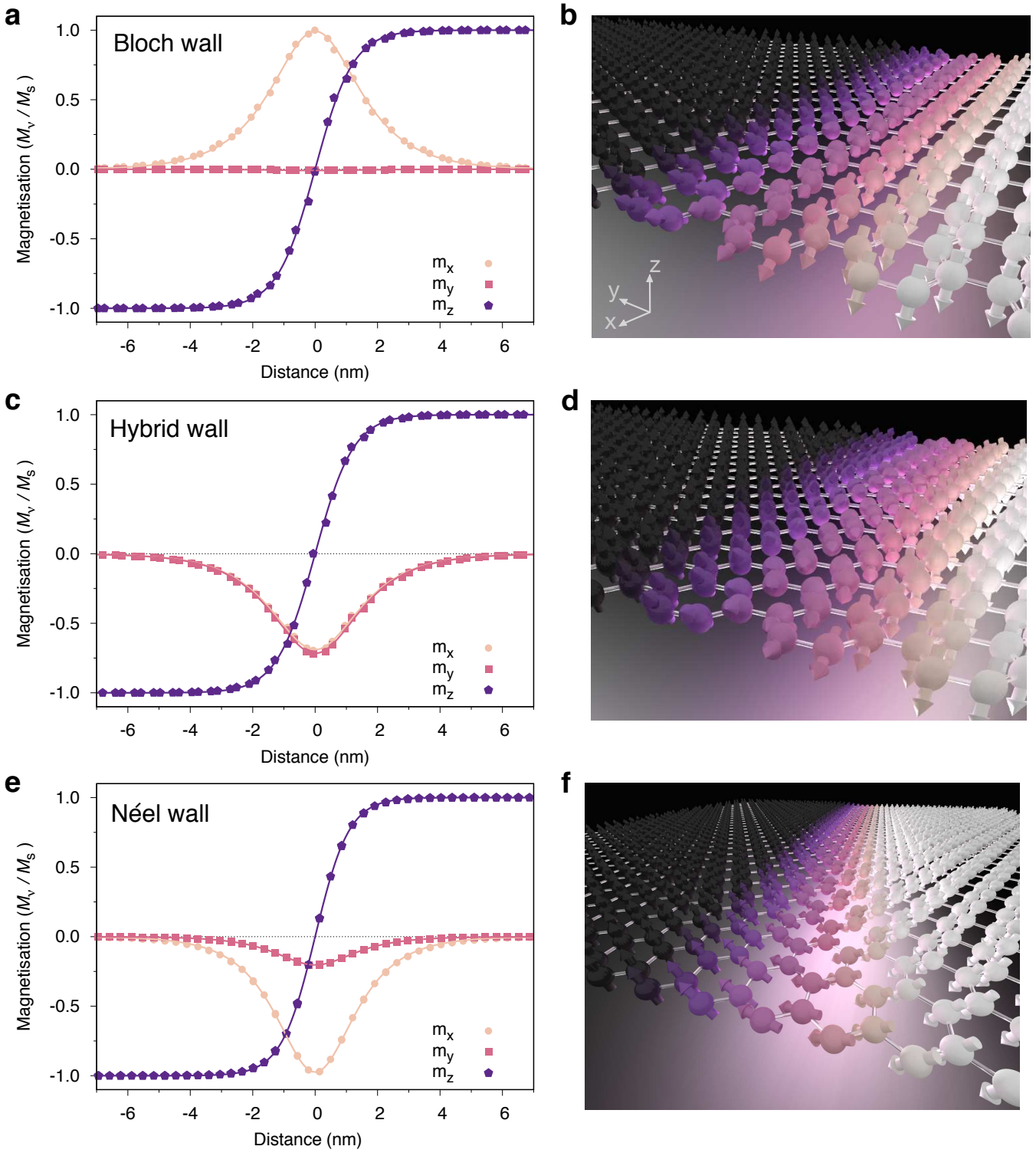
a
Bloch wall
Magnetisation (M_v / M_s)
Distance (nm)
m_x
m_y
m_z
b
z
y
x
c
Hybrid wall
Magnetisation (M_v / M_s)
Distance (nm)
m_x
m_y
m_z
d
e
Néel wall
Magnetisation (M_v / M_s)
Distance (nm)
m_x
m_y
m_z
f

Figure 3

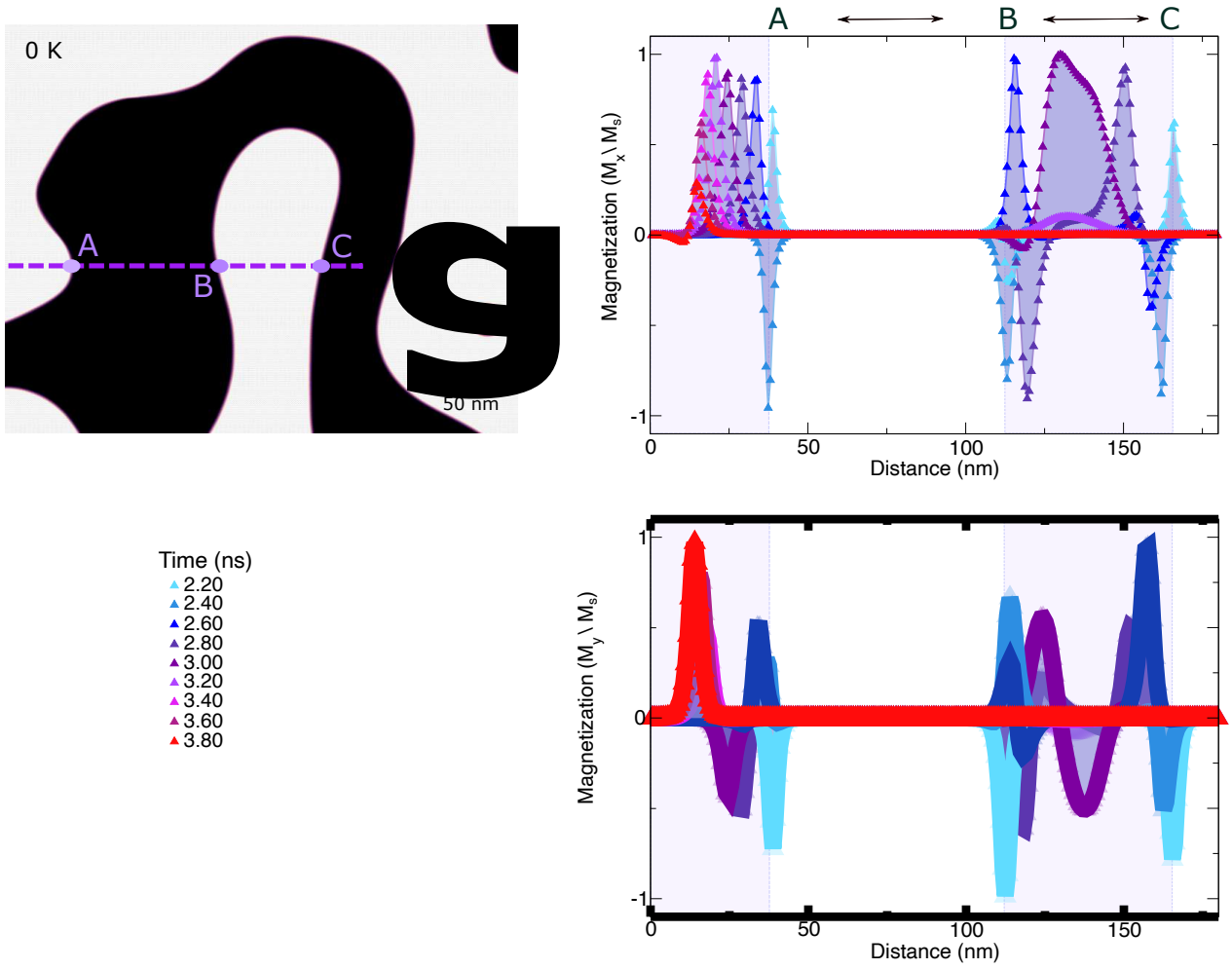
0 K
A
B
C
50 nm
A
B
C
Magnetization (M_x \ M_s)
Distance (nm)
Time (ns)
2.20
2.40
2.60
2.80
3.00
3.20
3.40
3.60
3.80
Magnetization (M_y \ M_s)
Distance (nm)

Figure 4